Analyst

PAPER

View Article Online
View Journal | View Issue

Cite this: *Analyst*, 2017, **142**, 326

Metal oxide semiconductor SERS-active substrates by defect engineering†

Hao Wu,[a] Hua Wang[a,b] and Guanghai Li*[a,b]

A general route to transform metal oxide semiconductors from non-SERS active to SERS-active substrates based on defect engineering is reported. The SERS enhancement factor (EF) of metal oxide semiconductors like α-MoO_3 and V_2O_5 can be greatly enhanced and the SERS performance can be optimized according to the detecting analyte and activating laser wavelength by introducing oxygen vacancy defects. The EF of R6G on α-MoO_{3-x} nanobelts can be as high as 1.8×10^7 with a detection limit of 10^{-8} M, which is the best among metal oxide semiconductors and comparable to noble metals without a "hot spot". A model, named "effective electric current model", was proposed to describe the photo-induced charge transfer process between the absorbed molecules and semiconductor substrates. The EF of 4-MBA, R6G and MB on α-MoO_{3-x} nanobelts with different oxygen vacancy concentrations calculated based on the model matches very well with experimental results. As an extension, some potential metal oxide semiconductor SERS-active substrates were predicted based on the model. Our results clearly demonstrate that, through defect engineering, the metal oxide semiconductors can be made SERS-active substrates with high stability and high biocompatibility.

Received 1st September 2016,
Accepted 23rd November 2016

DOI: 10.1039/c6an01959e

www.rsc.org/analyst

Introduction

Surface-enhanced Raman scattering (SERS) is a powerful tool for detecting trace-level molecules,[1–4] and has attracted a great deal of attention in different fields. Generally, there are two important mechanisms underlying the SERS enhancement, the electromagnetic mechanism (EM) and the chemical mechanism (CM).[5,6] In the EM, incident light induces surface plasmon resonance (SPR) on the substrate, producing a large enhancement in the Raman scattering.[7,8] While in the CM, apart from the situation where the surface enhanced resonance Raman scattering takes place in the molecule–substrate complex, one of the most widely-accepted interpretations considers that the molecular polarizability tensor is significantly enhanced because of the photo-induced charge transfer (PICT) process between the absorbed molecules and the substrate.[9] This PICT takes place at the molecular monolayer on the substrate.[10] Although noble SERS substrates/tags with highly uniform SERS signals have been widely developed,[11,12] the major challenge in SERS application is the controllable synthesis of a SERS-active substrate with a large enhancement factor.[4,11–13] It has been recognized that not only noble- and transition-metals exhibit the SERS effect,[14–17] but also some semiconductor materials display a notable SERS activity, for example, NiO, Cu_2O, Ag_2O, AgX (X = Cl, Br, I), ZnO, TiO_2, α-Fe_2O_3, Si, Ge, graphene and InAs/GaAs quantum dots.[9,10,18–33] The enhancement of Raman signals consists of both EM and CM mechanisms for metal SERS-active substrates, while it is usually only the CM mechanism for semiconductor SERS-active substrates. The semiconductor substrate not only can be used to increase the enhancement factor of the electromagnetic enhanced noble metal substrates, but also can be used as sensors in biological detection because of their high stability and biocompatibility.[18,34,35] Novel surface properties, high chemical stability, diversity of active substrates and controllable photoelectrical properties, as well as low cost and diverse synthetic techniques, make semiconductor substrates particularly important for their application in SERS.[10] The semiconductor substrate generally has a higher SERS uniformity than a noble metal substrate, and is suitable for a rapid SERS detection. The preparation of a semiconductor SERS-active substrate is relatively simple because the precise position of adjacent substrate nanoparticles is not crucial. Nevertheless, the application of semiconductor SERS-active substrates is limited because of

[a]*Key Laboratory of Materials Physics, Anhui Key Laboratory of Nanomaterials and Nanotechnology, Institute of Solid State Physics, Chinese Academy of Sciences, Hefei 230031, P. R. China. E-mail: ghli@issp.ac.cn; Fax: +86-551-65591434*

[b]*School of Chemistry and Materials Science, University of Science and Technology of China, Hefei 230031, P.R. China*

†Electronic supplementary information (ESI) available: The "effective electric current model" and its applications, details of α-MoO_3 and V_2O_5 samples and their SERS performance, point-to-point SERS mapping images of R6G over α-MoO_{3-x} nanobelts, HOMO and LUMO calculations of MB molecules, predicted potential metal oxide SERS-active substrates and evidence of SERS-activity from the chemical enhancement mechanism. See DOI: 10.1039/c6an01959e

their inferior performance in enhancement, a deficiency of candidates and the absence of regulation in exploring new semiconductor SERS-active materials.[19,35,36] The semiconductor materials explored so far usually only work for limited organic molecules because the PICT process takes place only when certain conditions are fulfilled, which is also an obstacle.

Recently, it was found that oxygen vacancies can increase the enhancement factor of nonstoichiometric tungsten oxide to as high as 3.4×10^5, which is the highest enhancement factor in semiconductors reported in the literature,[37] although the enhancement cannot be proved to be caused only by oxygen vacancies because of different structures of the substrates. Nevertheless, this result indeed provides a new avenue to efficiently improve the SERS enhancement of metal oxide semiconductors for practical applications. In this paper, we demonstrate a general route to anticipate the SERS activity of metal oxide semiconductors and transform the metal oxide semiconductor from non-SERS active to SERS active based on defect engineering, and provide a new method to detect different kinds of organics by controlling only the oxygen vacancy concentration without interfering with the crystal structure of the substrate. Using this route, α-MoO_3 (and α-V_2O_5 in part 4 of the ESI†), a non-SERS or weak SERS active substrate, can be transformed into a SERS-active substrate with an enhancement factor as high as 1.8×10^7 and a detection limit of 10^{-8} M for R6G, which is the highest among the reported SERS-active semiconductors. A simple model based on the effective electric current in the PICT was proposed to describe the PICT process and the oxygen vacancy concentration-dependent SERS enhancement of the oxide semiconductor substrate for the first time, which can be used to predict the SERS behaviours of other semiconductors. Our results not only can help to understand the SERS enhancement mechanism of semiconductor substrates, but also provides a strategy to design efficient semiconductor SERS-active substrates.

Experimental

Synthetic procedures

α-MoO_{3-x} nanobelts were synthesized by the hydrothermal method. In a typical procedure, 0.1 mmol $(NH_4)_6Mo_7O_{24}{\cdot}4H_2O$ (A.R. grade, ≥99.0%) was dissolved in 20 mL distilled water. Nitric acid (4 mol L^{-1}) was added drop by drop into the solution under magnetic stirring at room temperature until the pH value reached 1.0. Then the solution was sealed in a 50 mL Teflon-lined stainless autoclave at 453 K for 5 h. The white products were collected and washed several times with deionized water, centrifuged, and dried under vacuum at 353 K for 12 h. Subsequent annealing treatments were performed to achieve different oxygen vacancy concentrations (details can be found in part 3 of the ESI†). Stoichiometric α-MoO_3 microsized particles were prepared simply by calcination of $(NH_4)_6Mo_7O_{24}{\cdot}4H_2O$ (A.R. grade, ≥99.0%) at 973 K in air for 2 h and then collected through centrifugation in ethanol and dried in air at 353 K for 12 h.

Characterization methods

X-ray diffraction (XRD, Philips X'Pert Pro MPD and Cu Kα radiation), field-emission scanning electron microscopy (FESEM, Sirion 200 operating with an accelerating voltage of 10 kV), UV/VIS/NIR spectroscopy (Varian Cary-5E spectrophotometer) and transmission electron microscopy (TEM, JEOL model 2010) were employed for the characterization and DRS spectra measurements of the samples. X-ray photoelectron spectroscopy (XPS, Thermo ESCALAB250Xi) was used to determine the valence state and oxygen vacancy content. A confocal microprobe Raman spectrometer (Renishaw Invia Reflex) equipped with 532, 633 and 785 nm laser lines was used to record the Raman spectra. The data acquisition involved a sum of ten times 1 second accumulation with the power of about 0.3 mW modulated by the attenuator and at the spot size of 4 μm in diameter focused by the Leica objective.

Preparation of samples for Raman measurements

4-Mercaptobenzoic acid (4-MBA), Rhodamine 6G (R6G) and methylene blue (MB) were used as purchased without further purification. The other chemicals were all of analytical grade and were used without further purification. Triply distilled water was used in all experiments. The analytes were decorated on substrates by dispersing α-MoO_3 MPs or nonobelts into ethanol (for 4-MBA) or aqueous solution (for R6G and MB) of different mole concentrations at room temperature for 5 h with stirring. The excess molecules were rinsed off the samples with ethanol and deionized water through centrifugation. Then the MPs or NPs were dispersed into deionized water and sprayed on clean glass slides. To avoid the influence of photocatalysis, the whole process was operated in the dark.

Effective electric current model

The general consideration of how to transform a non-SERS active substrate into a SERS-active one with an optimal SERS performance when molecules are closely attached to the substrate with defects as the donor can be found in part 1 of the ESI.†

When electrons are excited from the substrate to the absorbed molecule, the potential in the molecule and the position of the nuclei of the atoms in the molecule will change. After these electrons tunnelled back to the substrate, the molecule will be in a vibrationally excited state and the polarization tensor of the molecule will be magnified.[38] Although the magnification is different for different vibration modes of the molecular SERS spectrum, the more the electrons jump onto molecular energy levels above the LUMO, the more the molecules are in the vibrationally excited state in the same period of time, and the more intensive all the molecular vibration signals can be. The current injected onto molecular energy levels above the LUMO is proportional to the enhancement factor of all the vibration modes of the molecular SERS spectrum in the PICT. Therefore, we can build our model by

focusing on the current injected onto molecular levels above the LUMO.

The possible PICT process can be divided into three sub-PICT processes: CT_1, CT_2 and CT_3, as shown in Scheme S3.† The actual PICT process consists of one to three of these sub-PICT processes. The CT_1 process is the PICT resonance between the doping levels and the coupled molecular levels above LUMO, the CT_2 process is the PICT resonance between the uncoupled energy levels in the conduction band of the substrate and the coupled molecular levels above LUMO, and the CT_3 process originates from the molecular resonance Raman scattering (RRS) and vibronic coupling between the molecular excited states and the conduction band states of the substrate.

The relationship between the defect concentration (M_t) and the SERS signal intensity (I_i, i = 1, 2) in the sub-PICT can be found in part 2 of the ESI.† For the CT_1 process, $I_1 = a \times M_t$, where the coefficient a is a constant when M_t is very small and is determined by the parameters of the excitation light, temperature, the adsorbed molecules and the substrate. If the coefficient is positive, the enhancement factor (EF) linearly increases with M_t. Otherwise no CT_1 exists. For the CT_2 process, the relationship can be written as

$$I_2 = \frac{{M_t}^2 + a_1 M_t + a_2}{b_1 M_t + b_2} \quad (1)$$

when M_t is very small. The coefficients a_i and b_i (i = 1, 2, 3 and 4) are also independent constants, which also can be determined using the above-mentioned parameters. Acting as donors in the semiconductor substrate, the defects are not involved in CT_3, and thus the SERS signal intensity in CT_3 (I_3) is a constant independent of the defect concentration.

Results and discussion

In the following, we will take MoO_3 as an example to show how to transform metal oxide semiconductors from a non-SERS active to a SERS-active substrate and optimize SERS performance based on our model.

MoO_3 exists in three polymorphs: the orthorhombic phase α-MoO_3,[39] monoclinic phase β-MoO_3,[40] and hexagonal phase h-MoO_3.[41] Surface plasmon cannot be excited by visible light in most semiconductor materials like α-MoO_3.[42] The CM mechanism is the only avenue to transform α-MoO_3 from non-SERS active to SERS active. Up to now, no report concerning the SERS of α-MoO_3 can be found in the literature. α-MoO_3 is a $4d^0$ Mo(VI) insulator with a bandgap of *ca.* 3.2 eV (see details in part 3 of the ESI†). The work function of stoichiometric α-MoO_3 is *ca.* 7.8 V.[43–45] Scheme 1a shows the energy diagram of band energy levels of a stoichiometric α-MoO_3 semiconductor,[43] together with energy levels of 4-mercaptobenzoic acid (4-MBA) (a fully protonated 4-MBA molecule was considered here for simplicity),[46] and methylene blue (MB, see calculations in part 6 of the ESI†) and Rhodamine 6G (R6G).[20] The energy levels of these three analytes coincide with M_3 and M_{12} in Scheme 1. The absorption spectra of the three analytes together with the excitation wavelength of the lasers used are shown in Fig. 1. One can see that the absorption band of 4-MBA is at the UV region whose energy is higher than the photon energy of all the excited lasers. The absorption band of R6G is at the green region, while that of MB is at the red region. The photon energy of the 532 nm laser is within and those of 633 and 785 nm lasers are lower than the energy level of the absorption band of R6G. The photon energy of 633 nm is within and those of 532 and 785 nm lasers are either higher or lower than the energy level of the absorption band of MB. Excitation with different laser wavelengths will result in different sub-PICT processes and different mechanisms of

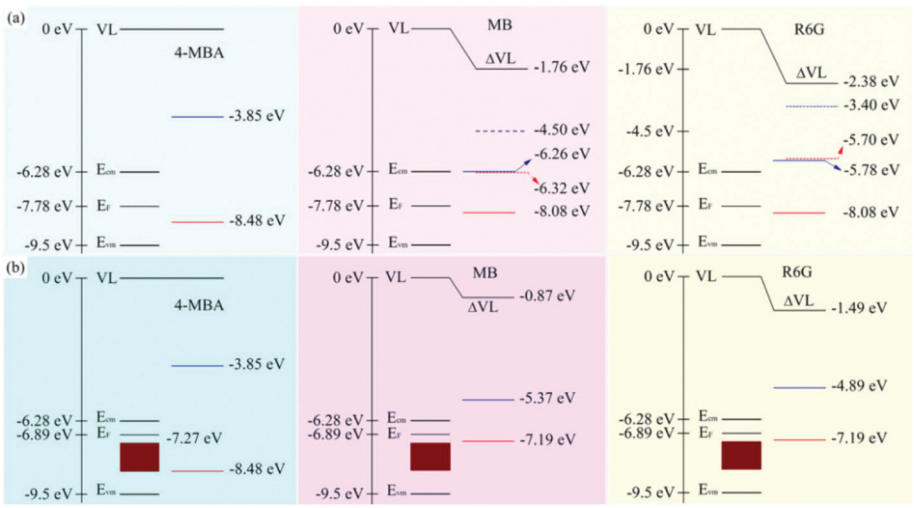

Scheme 1 Energy diagrams of 4-MBA, MB and R6G on α-MoO_3 before (a) and after (b) the introduction of defect levels. The navy blue line refers to the LUMO and the red line the HOMO, the wine color area represents the energy levels of oxygen vacancies. The dashed lines represent the LUMO and HOMO of MB and R6G if their vacuum levels align with the substrate.

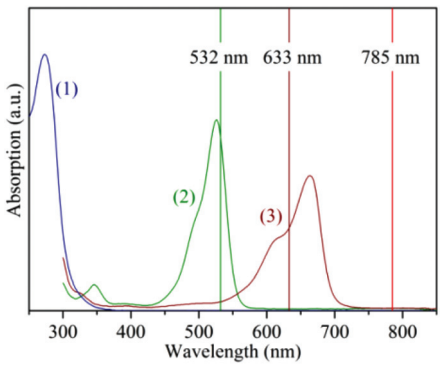

Fig. 1 Absorption spectra of 4-MBA (curve 1), R6G (2) and MB (3). The wavelength of the laser excitation is indicated by the vertical lines.

magnification of the molecular polarization tensor, as shown in Scheme 1a and Table 1.

From Table 1 one can see that the intrinsic stoichiometric α-MoO_3 semiconductor is a non-SERS active substrate for 4-MBA excited with these three lasers because the bandgap energy of α-MoO_3 and the energy gap (the difference between HOMO and LUMO) of 4-MBA are both larger than the laser photon energy. There is no energy matching, and the three above mentioned sub-PICT processes are all impossible. Therefore, no SERS enhancement would be observed for 4-MBA absorbed on stoichiometric α-MoO_3. The conduction band levels of α-MoO_3 and the energy gap of MB match with the laser photon energies of 532 and 633 nm, and thus the CT_3 process can take place. There is no energy matching among the 785 nm laser, α-MoO_3 and MB, and thus no sub-PICT process takes place and therefore no SERS effect can be observed for MB absorbed on α-MoO_3 excited with the 785 nm laser. The above analyses indicate that the stoichiometric α-MoO_3 is a SERS-active substrate for MB excited with 532 and 633 nm lasers and a non-SERS active substrate for MB excited with the 785 nm laser.

From Scheme 1a and Table 1, one also can see that the stoichiometric α-MoO_3 is a SERS-active substrate for R6G when excited with the 532 nm laser, in which the CT_3 process can take place, and the SERS effect will be strong enough to be detected. The photon energy and the energy gap of R6G being almost equal, a very strong RRS will occur from molecular HOMO directly to LUMO. Similarly, no sub-PICT process takes place because of the absence of the energy matching for R6G excited with 633 and 785 nm lasers. This analysis shows that the stoichiometric α-MoO_3 is a SERS-active substrate for R6G excited with the 532 nm laser and a non-SERS active substrate for R6G with 633 and 785 nm lasers.

Since oxygen vacancy defects unavoidably exist in all nanomaterials, the stoichiometric α-MoO_3 microsized particles (α-MoO_3 MPs) were used to verify the correctness of our model without defects. The oxygen vacancy defects in the α-MoO_3 MPs are much lower than those in nanomaterials like nanobelts and thus can be ignored (see part 4 of the ESI†). Fig. 2 shows the SERS spectra of 4-MBA, MB and R6G absorbed on the stoichiometric α-MoO_3 MPs excited with different laser wavelengths. From Fig. 2a one can see that, when excited with the 532 nm laser, no Raman signals can be observed for 10^{-3} M 4-MBA, while SERS signals can be observed for 10^{-5} M MB

Table 1 Energy level matching and sub-PICT process of 4-MBA, MB and R6G adsorbed on stoichiometric α-MoO_3 with different laser wavelengths

	4-MBA		MB		R6G	
Laser wavelength (nm)	Energy matching	Sub-PICT process	Energy matching	Sub-PICT process	Energy matching	Sub-PICT process
532 (2.33 eV)	None	None	$h\nu > E_{LUMO} - E_{HOMO}$ $h\nu > E_{cm} - E_{HOMO}$	CT_3	$h\nu > E_{LUMO} - E_{HOMO}$ $h\nu > E_{cm} - E_{HOMO}$	CT_3
633 (1.96 eV)	None	None	$h\nu > E_{LUMO} - E_{HOMO}$ $h\nu > E_{cm} - E_{HOMO}$	CT_3	None	None
785 (1.58 eV)	None	None	None	None	None	None

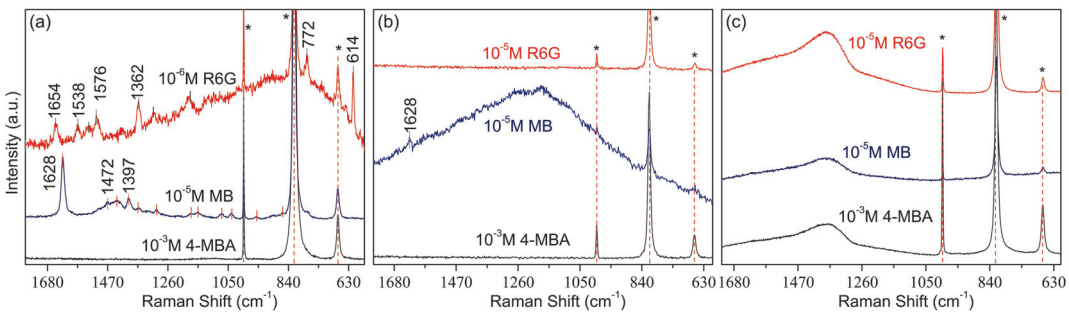

Fig. 2 SERS spectra of 4-MBA, MB and R6G on stoichiometric α-MoO_3 MPs excited with the laser wavelengths of (a) 532 nm, (b) 633 nm and (c) 785 nm lasers. The * refers to the Raman peaks from α-MoO_3. The molecular characteristic peak and molar concentration are indicated.

and 10^{-6} M R6G, which is in good agreement with the prediction shown in Table 1. The SERS enhancement of R6G is recognizable considering the 10^{-6} M concentration, owing to the contribution of the CT_3 process assisted by a strong RRS. There are no SERS signals for 10^{-5} M R6G and 10^{-3} M 4-MBA excited with the 633 nm laser, while only one weak recognizable peak remains for 10^{-5} M MB, as shown in Fig. 2b. No SERS signals can be detected for these three molecules excited with the 785 nm laser, as shown in Fig. 2c, which is in good agreement with the results shown in Table 1.

From the above analyses and experimental results, one can see that whether the stoichiometric α-MoO_3 MPs are SERS-active substrates depends on the excitation laser wavelength (or photon energy) and the detected molecules. As no defect levels are available, a possible sub-PICT process is the CT_3, and thus the stoichiometric α-MoO_3 MPs are non-SERS substrates except for R6G excited with the 532 nm laser and MB with 532 and 633 lasers. In the following discussion, we will demonstrate that, by introducing defect levels in the bandgap, the α-MoO_3 nanobelts become SERS-active substrates independent of the excitation laser wavelength and the detected molecules. The defect levels were introduced by oxygen vacancies instead of element doping, and the α-MoO_3 nanobelts are surface-clean without any surfactants, which can effectively suppress the interference from doping elements and other chemical compounds.

On the other hand, as the nanobelts are several tens of micrometers in length, about 200 nm in width and 20 nm in thickness, the influence of surface defects on SERS can be neglected. It was found that the introduction of oxygen vacancy defects in a low concentration has no notable influence on the absorption property of the α-MoO_3 nanobelts, as shown in part 4 of the ESI,† and thus the influence of the absorption property of the substrate on the SERS effect can be ignored.

The introduction of oxygen vacancies will form defect levels in the bandgap of the α-MoO_3 nanobelts, which will act as new valence bands (E_{V2} in Scheme S2†). The value of E_{vm} increases and the CT_1 and CT_2 will join the PICT process, and thus will obviously enhance the SERS effect, as shown in Scheme 1b. The energy level matching and the sub-PICT process of 4-MBA, MB and R6G adsorbed on the α-MoO_3 nanobelts excited with different laser wavelengths are shown in Table 2. From this table one can see that the α-MoO_3 nanobelts are SERS-active substrates for 4-MBA, MB and R6G excited with 532, 633 and 785 nm lasers except for 4-MBA with the 785 nm laser. For 4-MBA excited with the 532 nm laser, the PICT process consists of only CT_2, while for MB the PICT process consists of both CT_1 and CT_3, and for R6G the CT_1 and CT_3. When excited with the 633 nm laser, the PICT process consists of CT_1 and CT_3 for MB, and only CT_2 for 4-MBA and R6G. But when excited with the 785 nm laser, the only CT process is CT_2 for MB and R6G, and there is no PICT process for 4-MBA (the energetic difference between the LUMO of 4-MBA and the defect levels is larger than the energy of the two photons, and thus no notable sub-PICT process exists). The occurrence of the sub-PICT process means the observable SERS effect. It should be pointed out that with the 532 nm laser, the energy difference between the highest defect level and the LUMO of R6G equals the energy of photons, and a very strong PICT resonance between the substrate and R6G will occur.[47] This strong resonance between α-MoO_{3-x} nanobelts and R6G will make the CT_1 process much stronger than the previous CT_3 between stoichiometric α-MoO_3 MPs and R6G, which will enhance the SERS signals obviously.

The above analyses show that the introduction of oxygen vacancy defects will turn α-MoO_3 nanobelts from a non-SERS activity to a SERS activity substrate for 4-MBA with 532 and 633 nm lasers, improve the enhancement notably for MB with 532 and 633 nm lasers and transform α-MoO_3 from a non-SERS activity substrate to a SERS activity one for MB with 785 nm laser, improve the enhancement of α-MoO_3 for R6G with 532 nm laser and turn α-MoO_3 from a non-SERS active substrate to a SERS-active substrate for R6G with 633 and 785 nm lasers.

Fig. 3 shows the SERS spectra of 4-MBA, MB and R6G absorbed on the α-MoO_{3-x} nanobelt substrate excited with different laser wavelengths. Comparing with Fig. 2, one can see the SERS signals of the molecules on α-MoO_{3-x} nanobelts are much stronger than those on stoichiometric α-MoO_3 MPs. The SERS signals of MB and R6G can be observed with all the three lasers over α-MoO_{3-x} nanobelts. The SERS signals of R6G with 532 nm laser and MB with 532 and 633 nm lasers over α-MoO_{3-x} nanobelts are distinct and stronger than those over

Table 2 Energy level matching and sub-PICT process of 4-MBA, MB and R6G adsorbed on α-MoO_{3-x} nanobelts with different laser wavelengths

	4-MBA		MB		R6G	
Laser wavelength (nm)	Energy matching	Sub-PICT process	Energy matching	Sub-PICT process	Energy matching	Sub-PICT process
532 (2.33 eV)	$h\nu > E_{cm} - E_{vm}$	CT_2	$h\nu > E_{cm} - E_{vm}$ $h\nu > E_{LUMO} - E_{HOMO}$ $h\nu > E_{cm} - E_{HOMO}$	CT_1 CT_3	$h\nu > E_{cm} - E_{vm}$ $h\nu > E_{LUMO} - E_{HOMO}$ $h\nu > E_{cm} - E_{HOMO}$	CT_1 CT_3
633 (1.96 eV)	$h\nu > E_{cm} - E_{vm}$	CT_2	$h\nu > E_{cm} - E_{vm}$ $h\nu > E_{LUMO} - E_{HOMO}$ $h\nu > E_{cm} - E_{HOMO}$	CT_1 CT_3	$h\nu > E_{cm} - E_{vm}$	CT_2
785 (1.58 eV)	$h\nu > E_{cm} - E_{vm}$	None	$h\nu > E_{cm} - E_{vm}$	CT_2	$h\nu > E_{cm} - E_{vm}$	CT_2

stoichiometric α-MoO_3 MPs, demonstrating the effectiveness of introducing defect levels in improving SERS-activity. 4-MBA shows distinct SERS signals on α-MoO_{3-x} nanobelts with 532 and 633 nm lasers, proving the existence of the CT_2 process despite its relatively weak SERS enhancement. The appearance of distinct SERS signals with the 785 nm laser for 4-MBA on α-MoO_{3-x} nanobelts is unexpected according to our analysis listed in Table 2. This difference might originate from the assumption that $\gamma = 0$. In the system of 4-MBA and α-MoO_{3-x}, electrons from the highest of the CT_2-involved conduction bands of α-MoO_{3-x} can be transferred to the LUMO of 4-MBA with a tiny energy change γ of about 0.26 eV (calculated from: −3.85 eV − (−7.27 eV + 1.58 eV × 2)), leading to the CT_2 process.

It is worth noting that, by introducing oxygen vacancies, the α-MoO_3 MP substrate can also be transformed either from SERS-inactive to SERS-active or from a weak SERS-activity to a high SERS-activity substrate, see Fig. S7.† This result clearly demonstrates that the promotions of the SERS-activity of α-MoO_3 nanobelts are attributed to oxygen vacancy levels, and the influence of different specific surface areas between α-MoO_3 MPs and nanobelts can be excluded.

The above results clearly prove that not only an originally intrinsic non-SERS active α-MoO_3 substrate can be transformed into a SERS active substrate, but also the SERS performance can be enhanced by introducing defect energy levels into the bandgap of α-MoO_3 nanobelts. In the following, we will further optimize the SERS performance by controlling the oxygen vacancy concentration in the α-MoO_{3-x} nanobelts.

Eight α-MoO_{3-x} nanobelt samples with different oxygen vacancy concentrations (different x in α-MoO_{3-x}) were prepared (the preparation methods and oxygen vacancy concentration can be found in part 4 of the ESI†). Since there are no changes in the crystal structure, morphology and size of the nanobelts with different oxygen vacancy concentrations, the absorption property of these 8 samples can be regard as the same (see details in parts 4 of the ESI†), and thus the SERS enhancement factors of the 8 samples are comparable in the intensity of the corresponding characteristic Raman peaks.

The SERS spectra of 4-MBA, MB and R6G on α-MoO_{3-x} nanobelts with different oxygen vacancy concentrations excited with different lasers are shown in Fig. S8.† Clearly, the SERS enhancement of 4-MBA, MB and R6G depends on the oxygen vacancy concentration in the α-MoO_{3-x} nanobelts, and distinct and relatively strong SERS signals can be observed only with some oxygen vacancy concentrations. Additionally, the background fluorescence in the Raman spectrum can be eliminated with certain specific oxygen vacancy concentrations, which provides clear evidence that the PICT process has been promoted.[48]

Fig. 4 shows the dependence of the SERS enhancement of 4-MBA, MB and R6G on the oxygen vacancy concentration deduced from Fig. S8† using the intensity of the characteristic peak in each Raman spectrum (4-MBA with 633 and 785 lasers, R6G with the 785 nm laser was not given because only one sample has SERS enhancement in all 8 samples), in which two distinct features can be clearly seen. First, the Raman peak intensity firstly increases with increasing oxygen vacancy concentration, reaches the maximum value and then gradually decreases, and finally drops to a constant value (or zero) with further increasing the oxygen vacancy concentration. Second, the Raman peak intensity gradually decreases from the highest value till a constant value (or zero), and then remains at the constant value with further increasing the oxygen vacancy concentration. There are two or three stages in the relationship between the Raman peak intensity and the oxygen vacancy concentration. The best fittings of the experimental data are shown by the dashed lines in different colors in Fig. 4 (the error bars are multiple measurements from different parts of the substrate). The accurate values of the parameters in fitting functions are meaningless due to the different intensities of the SERS signals from different parts of the substrate. Nevertheless, the fitting functions indeed show the variation trend of the Raman peak intensity, and can be well explained by our model. It is worth noting that the point-to-point SERS mapping and the corresponding SERS intensity analysis of R6G at 614 cm^{-1} excited with the 532 nm laser demonstrate the high SERS uniformity of the α-MoO_{3-x} nanobelt substrate, as shown in Fig. S9,† in which the standard deviation of the measurements is about 12.2%.

Since the oxygen vacancy concentration is relatively low, the changes in the conduction band minimum, the valence band

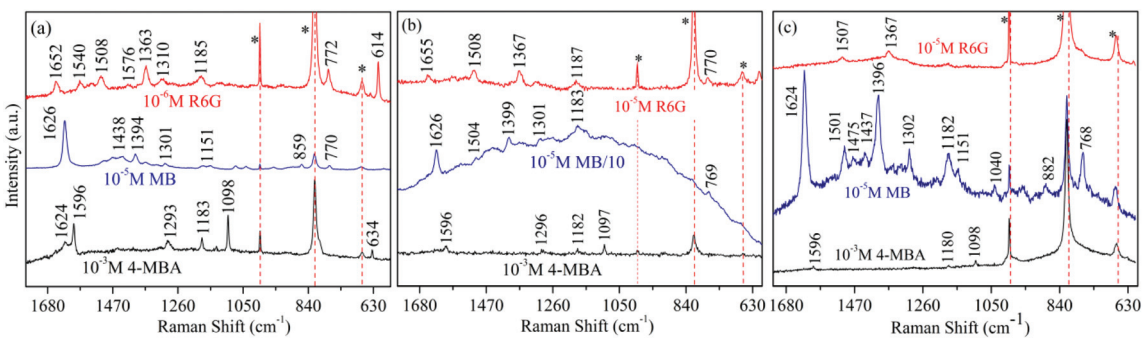

Fig. 3 SERS spectra of 4-MBA, MB and R6G on α-MoO_{3-x} nanobelts excited with the laser wavelengths of (a) 532 nm, (b) 633 nm and (c) 785 nm.

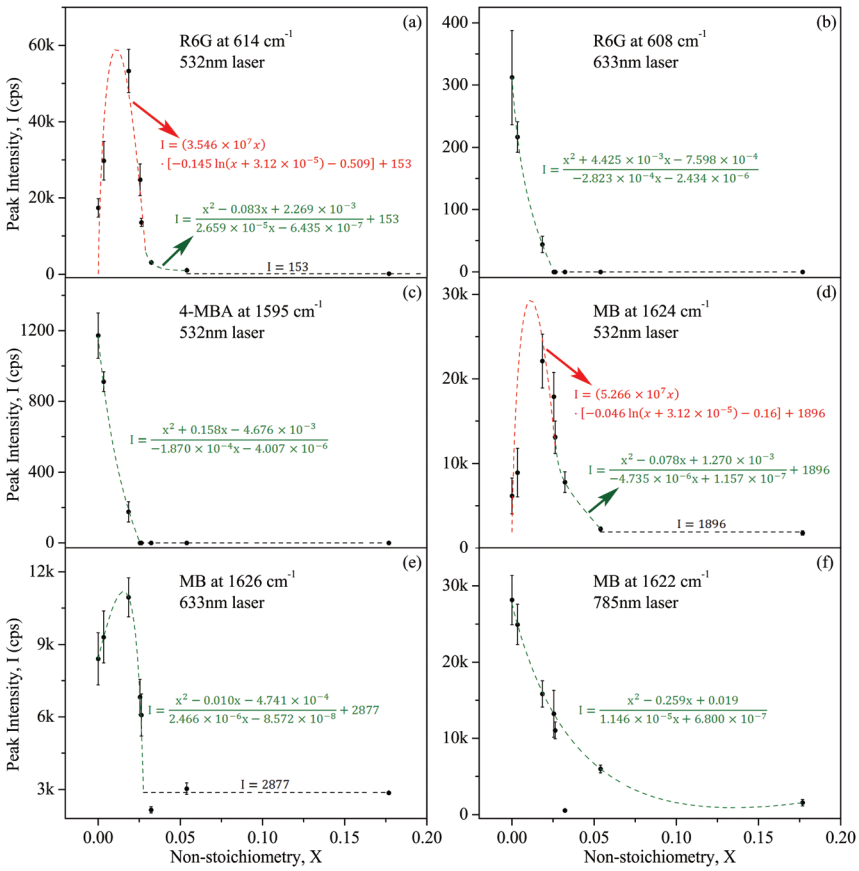

Fig. 4 Dependence of SERS enhancement of 4-MBA, R6G and MB on oxygen vacancy concentration over α-MoO_{3-x} nanobelts excited with different laser wavelengths. The dashed lines are the fitting results from our model together with the fitting functions.

maximum and the highest/lowest defect levels in the α-MoO_{3-x} nanobelts with increasing oxygen vacancy concentration are ignorable. But the change in Fermi energy cannot be ignored, which is an important factor to be considered. Defect levels will change the position of Fermi levels of the α-MoO_{3-x} nanobelts, leading to variations in the molecular LUMO or HOMO levels relative to the α-MoO_{3-x} nanobelts if these levels are pinned to the Fermi level of the α-MoO_{3-x} nanobelts, which in turn will change the pattern of the sub-PICT process, resulting in different sub-PICT processes. Therefore, there are several stages in which different sub-PICT processes are dominant. The HOMOs of MB and R6G are pinned under the Fermi level of the α-MoO_{3-x} nanobelts, and E_{HOMO} and E_{LUMO} can be calculated using $E_{HOMO} = E_{CM} - h(x) - 0.3$ eV, $E_{LUMO} = E_{CM} - h(x) + (E_{LUMO} - E_{HOMO}) - 0.3$ eV, where E_{CM} is the energy at the bottom of the conduction band of the α-MoO_{3-x} nanobelts, $h(x) = 0.184 - 0.016\ln(x + 3.12 \times 10^{-5})$ is the function of the energy difference between the Fermi level and the upper conduction band bottom, which is a function of the non-stoichiometry, x. $E_{LUMO} - E_{HOMO}$ is the energy difference between molecular HOMO and LUMO and is independent of the oxygen vacancy concentration.

For R6G with a 532 nm laser, the PICT process contains CT_1, CT_2 and CT_3. The PICT process of R6G molecules absorbed on α-MoO_{3-x} nanobelts can be divided into three stages for different oxygen vacancy concentrations. At the first stage ($0 < x < 0.02631$, the dashed red line), CT_1 and CT_3 dominate the PICT process. According to our model, the Raman peak intensity in this stage can be written as $I = I_1 + I_3 = aM_t + b$. Here, M_t is the oxygen vacancy concentration and is proportional to the non-stoichiometry, x. After merging the constant coefficients, the relationship between the molecular Raman intensity and the non-stoichiometry of α-MoO_{3-x} nanobelts can be written as $I = ax + b$. Considering that only defect levels whose energy is in the interval of $[E_{LUMO} - h\nu - \gamma, E_2]$ will be involved in the CT_1 process (Scheme S4a†), where $h\nu$ represents the photon energy and γ is about 0.42 eV, the Raman peak intensity can be written as (see details in part 2 of the ESI†):

$$I = a\varphi(x)x + b \tag{2}$$

where $a\varphi(x)x$ is the contribution from the CT_1, and b is the contribution from the CT_3, a and b are constants, and $b = 152$. The factor $\varphi(x)$ is the proportion of available defect levels in the CT_1 process:

$$\varphi(x) = -0.145\ \ln(x + 3.12 \times 10^{-5}) - 0.509 \quad 0 \le x \le 0.02631 \tag{3}$$

Therefore the peak intensity can be written as

$$I = -a\{0.145\ \ln(x + 3.12 \times 10^{-5}) + 0.509\}x + 152 \quad 0 \le x \le 0.02631 \tag{4}$$

Eqn (4) can well fit the experimental data (see the red dashed line in Fig. 4a).

From eqn (3), one can see that when x = 0.02631, $\varphi(x)$ = 0, CT_1 disappears, and the PICT process enters stage II (0.02631 < x < 0.05387). In this stage, the PICT process contains only CT_2 and CT_3. From Scheme S4a† and a very slight change in the E_{LUMO} value (from −4.52 to −4.51 eV, calculated using the equation: $E_{LUMO} = E_{CM} - h(x) + (E_{LUMO} - E_{HOMO}) - 0.3$ eV), one can conclude that all the defect levels will be involved in the CT_2 process, and in this case $\varphi(x)$ = 1. The Raman peak intensity can be written as:

$$I = \frac{x^2 + a_1x + a_2}{b_1x + b_2} + 152 \tag{5}$$

where a_i and b_i (i = 1, 2) are constants, and the constant 152 is the contribution from the CT_3. Eqn (5) also fits the experimental data perfectly, as shown by the olive dashed line in Fig. 4a. At the third stage (x > 0.05387), the CT_2 process disappears, and the PICT process contains only CT_3, thus the Raman peak intensity is a constant (I = 152), as shown by the black dashed line in Fig. 4a. A similar fitting can be found in part 2 of the ESI† for R6G with the other two lasers as well as for MB and 4-MBA with the three lasers used; the fitting results are shown in Fig. 4b–f.

It is worth noting that some data are beyond the fitting line, revealing that other factors might affect the PICT process. In our model, we suppose that the photo-induced electrons do not affect the Fermi level E_F of the substrate, and the original E_F of α-MoO_{3-x} nanobelts was used instead of that under laser light, which could be the reason for the deviation. On the other hand, our model is based on a very small M_t, and a deviation of experimental data from the model can be expected at higher values of M_t.

From the above results, one can see that the SERS intensity of 4-MBA, MB and R6G can be greatly enhanced in the α-MoO_{3-x} nanobelts with an appropriate oxygen vacancy concentration. Fig. 5 shows the SERS spectra of 4-MBA, MB and R6G with the lowest detecting concentration on the α-MoO_{3-x} nanobelts with the optimal oxygen vacancy concentration. Table S4 in part 7 of the ESI† lists the enhancement factors, detection limits and the optimal oxygen vacancy concentrations for 4-MBA, MB and R6G on the α-MoO_{3-x} nanobelts. Since a high concentration of the adsorbate usually leads to a higher proportion of non-monolayer adsorption and thus a lower EF, the enhancement factors of the same adsorbate in different concentrations, is usually slightly different, which is considered the reason for the reported concentration-dependent EF in $W_{18}O_{49}$.[37] Therefore the enhancement factors in this study were calculated using the concentrations at the detection limits. From Table S4† one can see that the enhancement factor can reach as high as 295, 1.0×10^6 and 1.8×10^7 for 4-MBA, MB and R6G, respectively. The detection limit of R6G is as low as 10^{-8} M, which is the lowest detection limit in the semiconductor SERS substrate reported in the literature, and is comparable to noble metals. This huge enhancement confirms the conclusion proposed by Lombardi that the most intensive SERS enhancement occurs in transitions terminating at the band edges (the PICT resonance between the highest defect level and molecular LUMO here).[47] Since the energy difference between the highest defect level in α-MoO_{3-x} and the LUMO of R6G is just equal to the energy of photons (considering γ), the enhancement factor of 1.8×10^7 is achieved with the assistance of the strongest PICT resonance and the optimization of oxygen vacancy defects.

The above results clearly demonstrate that through defect engineering, the SERS signals of molecules on a metal oxide semiconductor substrate can be substantially enhanced, and a non-SERS or weak SERS active substrate can be transformed into a SERS-active substrate. In the ESI† we provided further evidence that V_2O_5 nanoparticles, a weak SERS active substrate with the 532 nm laser and a non-SERS substrate with 633 and 785 nm lasers for R6G, can be transformed into a SERS-active substrate with all three lasers by defect engineering. Because of the absence of CT_1 and CT_3, the SERS enhancement of 4-MBA on the α-MoO_{3-x} nanobelt substrate is relatively weak. The CT_3 process cannot take place in wide energy gap molecules like 4-MBA. Theoretically, defect levels can locate on any position in the bandgap of a semiconductor, and thus the CT_1 process can occur through defect engineering. For 4-MBA, the

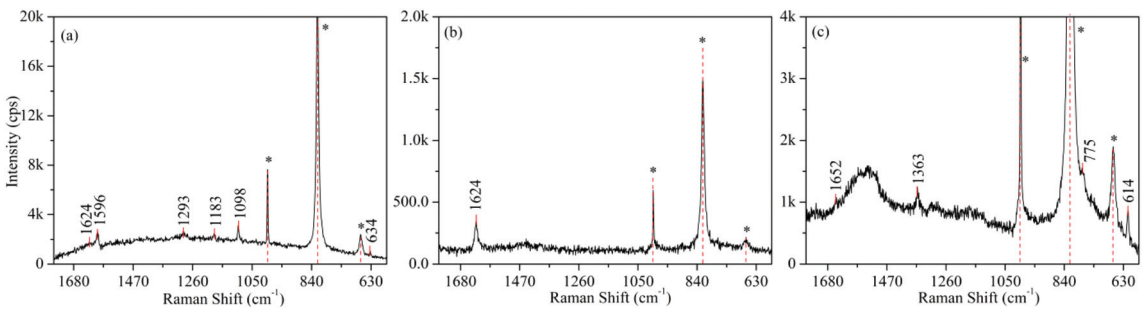

Fig. 5 SERS spectra on the optimal α-MoO_{3-x} nanobelt substrate excited with the 532 nm laser. (a) 4-MBA: 10^{-3} M, $x \sim 0$, (b) MB: 10^{-7} M, x = 0.01851 and (c) R6G: 10^{-8} M, x = 0.01851.

CT_1 process will appear if some of the energy levels in the conduction band of the α-MoO_{3-x} nanobelts have been remarkably occupied, which can be realized either by increasing the oxygen vacancy concentration to a very high level or by element doping. However, high oxygen vacancy concentrations will affect the crystal structure of the substrate, while element doping will bring in other influential factors, which will not be discussed here.

To reduce errors in recording the molecular Raman peak intensity, excess molecules on the substrate (MoO_3 and V_2O_5) have been rinsed off with deionized water and ethanol. Therefore the Raman intensities are relatively weakened. In practical applications, by dropping the molecular solution directly onto the MoO_{3-x} nanobelt substrate, an even stronger SERS enhancement can be seen.

From the effective electric current model we can propose some potential metal oxide candidates as SERS-active substrates. Taking R6G excited with the 532 nm laser as an example, we predict that the stoichiometric Cr_2O_3, CrO_3, Co_3O_4, CoO, and Ta_2O_5 are SERS-active substrates, and the oxygen vacancy defects can obviously enhance the SERS-activity of CrO_3 and Ta_2O_5, as shown in part 7 of the ESI.†

Conclusions

The realization of a semiconductor SERS-active substrate depends on the thermodynamically allowed PICT process between the substrate and the adsorbed molecules after considering the energy level realignment. The PICT process can take place if the energy levels of the substrate and molecules match the excited light. In most cases, this condition is not fulfilled, and introducing energy levels like oxygen vacancy levels into the bandgap of the semiconductor is essential to realize or strengthen the PICT process by adding more sub-PICT processes. The energy matching among the excitation light, substrate and molecules levels determines the dominant sub-PICT processes, and the sub-PICT processes involving the defect levels are affected remarkably by the defect concentration. By controlling the defect concentration, the SERS enhancement factor can be optimized substantially. Through defect engineering, the semiconductor SERS-active substrate and the detectable molecules can be greatly extended.

We proposed an effective electric current model based on the influence of oxygen vacancy defects on the current involved in the PICT. Our model not only can be used to quantitatively describe the PICT process and to anticipate the SERS activity of metal oxide semiconductors, but also can well explain our experimental data. Some metal oxide semiconductors that have not been studied so far can be promising SERS-active substrates based on our model.

By introducing oxygen vacancies, we have successfully transformed the non-SERS active α-MoO_3 to a SERS-active substrate, and optimized its SERS performance for 4-MBA, MB and R6G. The detection limits of R6G and MB on α-MoO_{3-x} nanobelts excited with the 532 nm laser can be as low as 10^{-8} and 10^{-7} M, respectively, demonstrating that the SERS performance of the α-MoO_{3-x} nanobelts is comparable with noble metal nanomaterials without the "hot spot". The semiconductor SERS-active substrate with high performance might find potential applications in different fields because of their high stability, high biocompatibility, high SERS uniformity and low cost compared to the widely used noble metals.

Acknowledgements

The authors would like to thank Prof. Wen Xu for his helpful discussion. This work was supported by the National Basic Research Program of China (Grant No. 2013CB934304).

References

1 L. B. Yang, P. Li, H. L. Liu, X. H. Tang and J. H. Liu, *Chem. Soc. Rev.*, 2015, **44**, 2837–2848.
2 U. S. Dinish, Z. G. Song, C. J. H. Ho, G. Balasundaram, A. B. E. Attia, X. M. Lu, B. Z. Tang, B. Liu and M. Olivo, *Adv. Funct. Mater.*, 2015, **25**, 2316–2325.
3 S. Nie and S. R. Emory, *Science*, 1997, **275**, 1102–1106.
4 Y. H. Lai, S. W. Chen, M. Hayashi, Y. J. Shiu, C. C. Huang, W. T. Chuang, C. J. Su, H. C. Jeng, J. W. Chang, Y. C. Lee, A. C. Su, C. Y. Mou and U. S. Jeng, *Adv. Funct. Mater.*, 2014, **24**, 2544–2552.
5 A. Campion and P. Kambhampati, *Chem. Soc. Rev.*, 1998, **27**, 241–250.
6 H. Ko, S. Singamaneni and V. V. Tsukruk, *Small*, 2008, **4**, 1576–1599.
7 G. Braun, I. Pavel, A. R. Morrill, D. S. Seferos, G. C. Bazan, N. O. Reich and M. Moskovits, *J. Am. Chem. Soc.*, 2007, **129**, 7760–7761.
8 F. Svedberg, Z. Li, H. Xu and M. Käll, *Nano Lett.*, 2006, **6**, 2639–2641.
9 A. Musumeci, D. Gosztola, T. Schiller, N. M. Dimitrijevic, V. Mujica, D. Martin and T. Rajh, *J. Am. Chem. Soc.*, 2009, **131**, 6040–6041.
10 W. Ji, B. Zhao and Y. Ozaki, *J. Raman Spectrosc.*, 2016, **47**, 51–58.
11 H. H. Wang, C. Y. Liu, S. B. Wu, N. W. Liu, C. Y. Peng, T. H. Chan, C. F. Hsu, J. K. Wang and Y. L. Wang, *Adv. Mater.*, 2006, **18**, 491–495.
12 B. Zhao, J. L. Shen, S. X. Chen, D. F. Wang, F. Li, S. Mathur, S. P. Song and C. H. Fan, *Chem. Sci.*, 2014, **5**, 4460–4466.
13 Y. H. Zheng, T. Thai, P. Reineck, L. Qiu, Y. M. Guo and U. Bach, *Adv. Funct. Mater.*, 2013, **23**, 1519–1526.
14 U. Wenning, B. Pettinger and H. Wetzel, *Chem. Phys. Lett.*, 1980, **70**, 49–54.
15 C. L. Haynes and R. P. Van Duyne, *Nano Lett.*, 2003, **3**, 939–943.
16 B. Ren, X.-F. Lin, Z.-L. Yang, G.-K. Liu, R. F. Aroca, B.-W. Mao and Z.-Q. Tian, *J. Am. Chem. Soc.*, 2003, **125**, 9598–9599.

17 L. Y. Chen, J. S. Yu, T. Fujita and M. W. Chen, *Adv. Funct. Mater.*, 2009, **19**, 1221–1226.
18 D. Y. Qi, L. J. Lu, L. Z. Wang and J. L. Zhang, *J. Am. Chem. Soc.*, 2014, **136**, 9886–9889.
19 M. T. Greiner, M. G. Helander, W. M. Tang, Z. B. Wang, J. Qiu and Z. H. Lu, *Nat. Mater.*, 2012, **11**, 76–81.
20 X. Ling, L. Xie, Y. Fang, H. Xu, H. Zhang, J. Kong, M. S. Dresselhaus, J. Zhang and Z. Liu, *Nano Lett.*, 2010, **10**, 553–561.
21 B. H. Loo, *Solid State Commun.*, 1982, **43**, 349–353.
22 B. Simic-Glavaski, *J. Phys. Chem.*, 1986, **90**, 3863–3865.
23 J. Wang, P. Zhang, T. He, H. Xin and F. Liu, *J. Phys. Chem.*, 1988, **92**, 1942–1945.
24 E. S. Brandt, *Appl. Spectrosc.*, 1993, **47**, 85–93.
25 X. Wang, T. He, H. Wen, C. Xu, J. Zuo and F.-C. Liu, *Spectrochim. Acta, Part A*, 1997, **53**, 1411–1417.
26 L. G. Quagliano, *J. Am. Chem. Soc.*, 2004, **126**, 7393–7398.
27 X. Fu, F. Bei, X. Wang, X. Yang and L. Lu, *J. Raman Spectrosc.*, 2009, **40**, 1290–1295.
28 Y. Wang, W. Ruan, J. Zhang, B. Yang, W. Xu, B. Zhao and J. R. Lombardi, *J. Raman Spectrosc.*, 2009, **40**, 1072–1077.
29 X. H. Li, G. Y. Chen, L. B. Yang, Z. Jin and J. H. Liu, *Adv. Funct. Mater.*, 2010, **20**, 2815–2824.
30 L. Jiang, P. G. Yin, T. T. You, H. Wang, X. F. Lang, L. Guo and S. H. Yang, *ChemPhysChem*, 2012, **13**, 3932–3936.
31 B. Dong, Y. Z. Huang, N. S. Yu, Y. R. Fang, B. S. Cao, Y. Z. Li, H. X. Xu and M. T. Sun, *Chem. – Asian J.*, 2010, **5**, 1824–1829.
32 J. S. Teguh, F. Liu, B. G. Xing and E. K. L. Yeow, *Chem. – Asian J.*, 2012, **7**, 975–981.
33 L. Jiang, T. T. You, P. G. Yin, Y. Shang, D. F. Zhang, L. Guo and S. H. Yang, *Nanoscale*, 2013, **5**, 2784–2789.
34 S. C. Xu, Y. X. Zhang, Y. Y. Luo, S. Wang, H. L. Ding, J. M. Xu and G. H. Li, *Analyst*, 2013, **138**, 4519–4525.
35 S. J. Hurst, H. C. Fry, D. J. Gosztola and T. Rajh, *J. Phys. Chem. C*, 2011, **115**, 620–630.
36 N. Valley, N. Greeneltch, R. P. Van Duyne and G. C. Schatz, *J. Phys. Chem. Lett.*, 2013, **4**, 2599–2604.
37 S. Cong, Y. Yuan, Z. Chen, J. Hou, M. Yang, Y. Su, Y. Zhang, L. Li, Q. Li, F. Geng and Z. Zhao, *Nat. Commun.*, 2015, **6**, 7800.
38 B. N. J. Persson, K. Zhao and Z. Zhang, *Phys. Rev. Lett.*, 2006, **96**, 207401.
39 P. F. Carcia and E. M. McCarron III, *Thin Solid Films*, 1987, **155**, 53–63.
40 E. M. McCarron, *J. Chem. Soc., Chem. Commun.*, 1986, 336–338.
41 E. M. McCarron, D. M. Thomas and J. C. Calabrese, *Inorg. Chem.*, 1987, **26**, 370–373.
42 J. R. Lombardi and R. L. Birke, *J. Phys. Chem. C*, 2008, **112**, 5605–5617.
43 M. T. Greiner, L. Chai, M. G. Helander, W. M. Tang and Z. H. Lu, *Adv. Funct. Mater.*, 2012, **22**, 4557–4568.
44 T. He, Y. Ma, Y. Cao, P. Jiang, X. Zhang, W. Yang and J. Yao, *Langmuir*, 2001, **17**, 8024–8027.
45 D. O. Scanlon, G. W. Watson, D. J. Payne, G. R. Atkinson, R. G. Egdell and D. S. L. Law, *J. Phys. Chem. C*, 2010, **114**, 4636–4645.
46 X. Xue, W. Ruan, L. Yang, W. Ji, Y. Xie, L. Chen, W. Song, B. Zhao and J. R. Lombardi, *J. Raman Spectrosc.*, 2012, **43**, 61–64.
47 J. R. Lombardi and R. L. Birke, *J. Phys. Chem. C*, 2014, **118**, 11120–11130.
48 X. Wang, W. Shi, G. She and L. Mu, *J. Am. Chem. Soc.*, 2011, **133**, 16518–16523.